Wiley
Advances in Condensed Matter Physics
Volume 2024, Article ID 8722867, 15 pages
https://doi.org/10.1155/2024/8722867

WILEY

Research Article

The Effect of Pressure Variations on the Electronic Structure, Phonon, and Superconducting Properties of Yttrium Hydrogen Selenide Compound

Tadesse Bekele Aredo, Megersa Wodajo Shura, Mesfin Asfaw Afrassa, Kumneger Tadele, and Fekadu Tolessa Maremi

Department of Applied Physics, School of Applied Natural Science, Adama Science and Technology University, Adama, P.O. Box 1888, Ethiopia

Correspondence should be addressed to Tadesse Bekele Aredo; tadesseb154@gmail.com

Received 12 April 2024; Revised 13 May 2024; Accepted 16 May 2024; Published 31 May 2024

Academic Editor: Sefer Bora Lisesivdin

The electronic, phonon, and superconducting properties of hexagonal yttrium hydrogen selenide (YHSe) are studied using density functional theory (DFT) methods. The DFT analysis revealed that the energy bandgap and density of states near the Fermi energy (ε_F) decrease with increasing pressure. Additionally, the influence of pressure on the vibrational properties of YHSe is also examined. The findings of the vibrational properties indicate a stiffening of lattice dynamics under pressure and the identification of negative Gruneisen parameters at certain high symmetry sites. This enhances and deepens the understanding of the vibrational characteristics of YHSe under extreme pressure conditions. Finally, the electron–phonon coupling (EPC) parameter (λ) is examined under different pressures. The examination of EPCs across varying pressures showed a significant increase from 0.826 (0 GPa) to 2.6287 (200 GPa), where an increase in this EPC is found to increase the superconducting critical temperature (T_c). Furthermore, the nonmonotonic relationship between the superconducting critical temperature (T_c) and external pressure (P) in the YHSe compound is observed. Initially, T_c decreases with increasing pressure and then begins to rise again, reaching its peak value at extreme pressure. These findings provide valuable insights into the pressure-dependent properties of YHSe and have important implications for the field of superconductivity in condensed matter physics.

1. Introduction

The field of superconductivity has witnessed significant advancements and garnered attention due to its distinct characteristics and diverse industrial applications [1, 2, 3, 4, 5, 6]. However, the requirement of extremely low temperatures for these properties to manifest severely restricts their practical application. Consequently, the pursuit of achieving superconductivity at higher temperatures, potentially even at room temperature, has long been a fiercely competitive objective within the realm of superconductivity [7, 8, 9]. This is one of the reasons why extensive research in this field has been conducted for more than a century [9].

Since 1968, there has been significant advancement in the realm of hydrogen-based superconductivity, which was initially proposed by Ashcroft. The idea suggests that pressurized hydrogen could exhibit high-temperature superconductivity because of its elevated phonons energy [10]. As a result, metallic hydrogen stands out as the primary contender for attaining high-T_c superconductivity due to its remarkably elevated phonon vibration frequency [11, 12, 13]. However, achieving hydrogen metallization, referred to as the Wigner–Huntington transition, usually demands exceptionally high pressures, which makes it challenging to explore its electrical characteristics linked with superconductivity in such environments. Ashcroft suggested that by incorporating extra elements into hydrogen, it could be precompressed, enabling the system to retain its metallic properties and display superconductivity at lower pressures [14]. Hence, metal hydrides emerge as leading contenders for achieving high-temperature superconductivity (T_c). Recently, simple binary hydrides with the highest predicted superconducting critical temperature Tc using density functional theory (DFT) include MgH_6

(260 K at 300 GPa) [15] CaH_6 (235 K at 150 GPa) [16], and YH_6 (264 K at 120 GPa) [17, 18] among others. However, Ashcroft's analysis indicates that DFT calculations have effectively discounted nearly all binary hydrides, with experimental validations corroborating these forecasts [19]. Consequently, various researchers have investigated different binary hydrides using DFT and experimental methods, such as hydrogen sulfide (H_2S) and lanthanum super hydride LaH_{10} [20], which can manifest superconductivity at relatively elevated temperatures under extreme pressure circumstances.

While there has been extensive research into binary superconducting hydrides, the investigation into multicomponent superconducting hydrides has been comparatively limited. Nevertheless, the broader array of element combinations within multicomponent hydrides shows greater potential for achieving high-temperature superconductivity [21]. Recent experiments have revealed that ternary metal alloy hydrides demonstrate enhanced superconductivity when compared to their binary counterparts, such as (La, Y)H_6 [22] and (La, Y)H_{10} [22]. Additionally, theoretical analysis indicates that the ternary La and Y hydrides-based system holds considerable promise for achieving high critical temperatures of superconductivity [23].

Therefore, the major goal of this work was to conduct a theoretical examination of high-temperature superconductivity (T_c) caused by electron interactions with a crystal lattice. It mainly focuses on specific physical systems in which hydrogen plays an important part in the process of obtaining zero resistance at temperatures greater than the boiling point of liquid nitrogen (77 K). Consequently, this study focused on examining the yttrium hydrogen selenide (YHSe) ternary hydride system, which has been comparatively underexplored, with the goal of assessing the electronic structure, phonon dynamics, and superconducting properties using DFT under varying pressure levels.

2. Computational Detail

The computations were conducted utilizing the framework of DFT within the Quantum Espresso package to investigate the electronic structure, phonon dynamics, and superconducting properties of the YHSe system. In this investigation, the electronic structure, phonon, and superconducting properties were examined under different pressure conditions. The chosen pseudo-potential type for this study was the norm-conserving pseudo-potential with a functional type of GGA Perdew–Burke–Ernzerhof [24]. The optimal crystal structure (Figure 1) at ambient pressure, with lattice values obtained for this investigation, $a = b = 3.8055$ Å and $c = 3.8744$ Å. A plane wave basis set with an energy cutoff of 100 Ry was employed to ensure more precise outcomes in analyzing the hexagonal structures of YHSe within the space group $P\bar{6}m2$. Reciprocal space integration was conducted using k-point sampling employing sets of special points derived from the standard k-points technique established by Monkhorst and Pack [25]. A mesh of $12 \times 12 \times 12$ k-points was utilized to enhance more accuracy following a convergence test for electronic Brillouin zone (BZ) integration within the hexagonal structures of

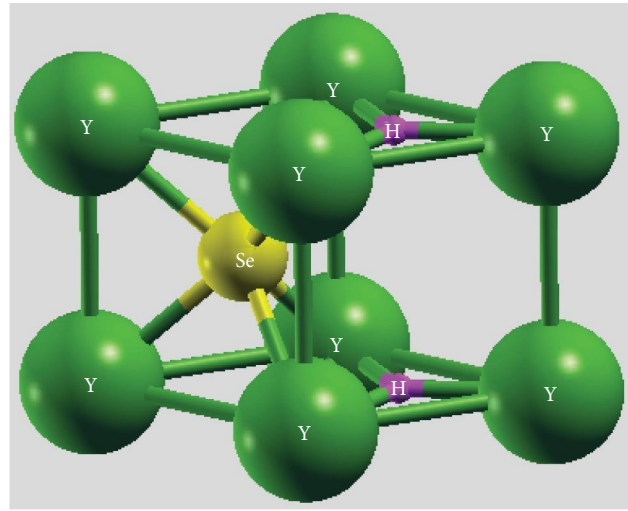

Figure 1: Optimized crystal structure of yttrium hydrogen selenide (YHSe) at 0 GPa.

YHSe. The structure's minimum total energy is attained through the automatic relaxation of internal coordinates, employing the Broyden–Fletcher–Goldfarb–Shanno algorithm [26]. This optimization process adheres to specific thresholds, ensuring an energy change of less than 0.000001 eV/atom. Moreover, the equilibrium atomic structure is fine-tuned by relaxing lattice atomic coordinates, maintaining a tolerance of less than 0.00001 eV/Å for each atom within the structure. These convergence tests meet the required standards for subsequent calculations. The phonon dispersion and superconducting properties were calculated using density functional perturbation theory implemented within the Quantum Espresso code [27]. The electron–phonon coupling (EPC) matrix elements were calculated within the first BZ using a $4 \times 4 \times 4$ q-mesh, while the individual EPC matrices were utilized with a $36 \times 36 \times 36$ k-points mesh for the YHSe system. Essentially, the Eliashberg theory spectral function relied on a dense distribution of k-points where in the dense k-points mesh encompassed all k and $k+q$ grid points, effectively ensuring coverage of the q-points mesh by the k-points mesh. The electronic structure, phonon dynamics, and superconducting properties were computed under pressure variation circumstances. We determined the superconducting transition temperature T_c by utilizing the Allen Dynes adapted McMillan equation [28] with the effective Coulomb pseudo-potential parameter ($\mu^* = 0.10$) [29]. The calculation of the critical temperature for superconductivity in a phonon-mediated superconductor can be conveniently expressed using a modified version of the McMillan [28] formula.

$$T_c = \frac{\omega_{\log}}{1.2} \exp\left(-\frac{1.04(1+\lambda)}{\lambda - \mu^*(1+0.6\lambda)}\right), \tag{1}$$

where μ^* represents the coulomb pseudo-potential, λ represents the EPC constant, and $\omega_{\log}$ stands for the logarithmic average phonon frequency. The EPC constant (λ) can be denoted as follows:

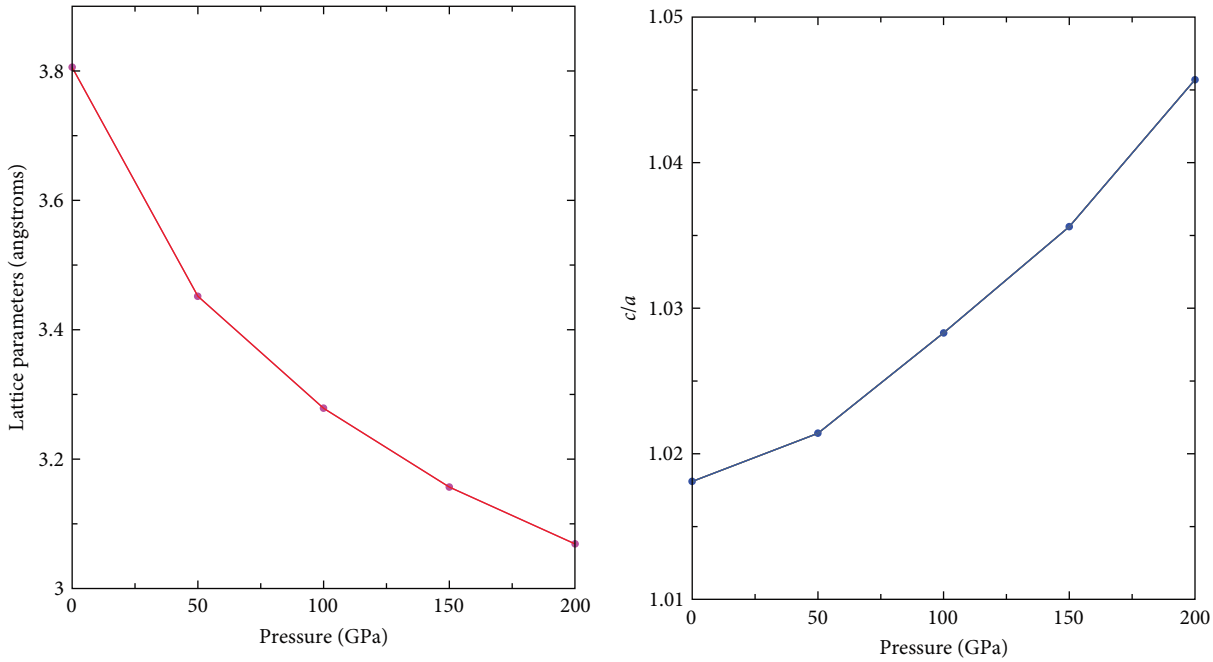

(a) (b)

FIGURE 2: (a) Calculated lattice parameters in angstroms and (b) the c/a ratio of hexagonal YHSe with space group P$\bar{6}$m2 under high pressure up to 200 GPa.

$$\lambda = 2\int_0^\infty \frac{\alpha^2 F(\omega)}{\omega} d\omega, \tag{2}$$

$$\omega_{\log} = \exp\left(\frac{2}{\lambda}\int_0^\infty \alpha^2 F(\omega)\frac{\ln(\omega)}{\omega} d\omega\right). \tag{3}$$

The ω parameter represents the frequency of phonons, while $\alpha^2 F(\omega)$ denotes the Eliashberg spectral function.

$$\alpha^2 F(\omega) = \frac{1}{2\pi N(\varepsilon_F)}\sum_{q\nu}\frac{\gamma_{q\nu}}{\omega_{q\nu}}\delta(\omega - \omega_{q\nu}), \tag{4}$$

where $N(\varepsilon_F)$ signifies the density of states (DOS) at the Fermi level per unit cell, where q-point denotes the wave vector, $\omega_{q\nu}$ represents the phonon frequency at the q-point, weighted with ν as the vibrational mode, $\varepsilon_{m,k}$ signifies the energy of the bare electronic Bloch state, ε_F represents the Fermi energy, g^{ν}_{mn} stands for the electron–phonon matrix element and $\gamma_{q\nu}$ represents the phonon line width, which can be formulated as follows:

$$\gamma_{q\nu} = \pi\omega_{q\nu}\sum_{mn}\sum_{k}|g^{\nu}_{mn}(k,q)|^2\delta(\varepsilon_{m,q+k} - \varepsilon_F)\delta(\varepsilon_{m,k} - \varepsilon_F), \tag{5}$$

$$g^{\nu}_{mn}(k,q) = \left(\frac{\hbar}{2M\omega_{q\nu}}\right)^{\frac{1}{2}} < m, k+q|\delta_{q\nu}V_{SCF}|n,k>. \tag{6}$$

Regarding the phonon-line width with the entirety of EPC can be articulated as follows:

$$\lambda = \sum_{k\nu}\lambda_{q\nu} = \sum_{k\nu}\frac{\gamma_{q\nu}}{2\pi N(\varepsilon_F)\omega^2_{q\nu}}. \tag{7}$$

From McMillan's [28] strong-coupling theory, the parameter describing the coupling between electrons and phonons can be formulated as follows:

$$\lambda = \frac{N(\varepsilon_F) < I^2 >}{M < \omega^2 >}, \tag{8}$$

where $< I^2 >$ the averaged over the Fermi surface represents the electron–phonon matrix element, with M denoting the atomic mass.

$$\langle\omega^2\rangle = \frac{2}{\lambda}\int_0^\infty \alpha^2 F(\omega)\omega d\omega. \tag{9}$$

3. Results and Discussion

3.1. Structural Properties. Because the material's structure is intricately connected to its other properties, our initial focus was on refining the unit-cell parameters of YHSe while subject to different pressure conditions. The table and accompanying figure present the optimized unit-cell parameters of YHSe's hexagonal crystal structure at pressures ranging from 0 to 200 GPa. Figure 2 illustrates the lattice parameters of hexagonal YHSe with space group P$\bar{6}$m2 under high pressure of up to 200 GPa. In this study, the observed decrease in lattice parameter with increasing pressure for YHSe can be attributed to the compressive effects of applied pressure on the crystal structure. In this finding, as pressure increases, the

Table 1: Calculated lattice parameters ($a = b$ and c) of hexagonal YHSe with space group P$\bar{6}$m2 under varying pressure conditions up to 200 GPa.

Pressure (GPa)	Lattice parameter $a = b$ (Å)	c (Å)
0	3.81	3.87
50	3.45	3.52
100	3.28	3.37
150	3.16	3.26
200	3.07	3.20

interatomic distances within the crystal lattice are reduced, leading to a contraction of the unit cell volume. The decrease in lattice parameters in this study indicates a higher packing density of atoms within the crystal lattice as pressure increases (Figure 2). Table 1 shows the lattice parameters (a and c) of hexagonal YHSe with space group P$\bar{6}$m2 under varying pressure conditions up to 200 GPa.

3.2. Electronic Properties. The study investigates the electronic properties of YHSe across varying pressures, focusing on its band structure and DOS. The analysis of the electronic properties of YHSe indicates that it is a semiconductor with a bandgap ranging from 1.24 to 1.51 eV under varying pressure. The band structure of hexagonal YHSe with space group P$\bar{6}$m2 was calculated by selecting specific k-points along the high symmetry path Γ–M–K-Γ–A–L–H [30]. Initially, at 0 GPa (see Figure 3(a)), YHSe has an indirect bandgap of 1.52 eV; the valance band maximum is located at the A-point, and the conduction band minimum is located at the Γ-point. Figure 4 depicts the indirect gaps at the Γ–Γ points decrease with increasing pressure, while those at the H–H points increase. Whereas the L–L gap initially increases up to 100 GPa, then decreases, and the M–M gap initially increases up to 150 GPa and then decreases at 200 GPa. Conversely, the direct gap decreases under pressure, with the gaps at K–K and A–A points also diminishing. Remarkably, at 0 GPa, the bandgap in the K-direction is direct, contrasting the Γ-point's behavior as it transformed into an indirect gap with increasing pressure, reversing the trend observed at the Γ-point. The band structure of YHSe (see Figures 3(a), 3(b), 3(c), 3(d), and 3(e)), calculated at each pressure, revealed that at ambient conditions, the highest point in the valence band is the A point. Initially, at 0 GPa, the lowest point in the conduction band is the Γ-point energy at Γ-point (1.15 eV), which has lower energy than the K (1.83 eV) and A (1.53 eV) points in the conduction band. However, as the pressure increases to 200 GPa, the lowest point shifts to the K-point (0.57 eV) in the conduction band, which has lower energy than the Γ-point (0.88 eV), A (0.68 eV), L (5.34 eV), and H (6.44 eV) points. These findings revealed that as pressure increases, the gaps between bands at Γ–Γ, A–A, and K–K in YHSe gradually decrease. Even when subjected to extreme pressure at 200 GPa, the distinct energies of the conduction and valence bands persist without overlapping. This indicates that YHSe is still a semiconductor characteristic that has a lower bandgap at extreme pressure. The band structure of YHSe calculated at 0 GPa is shown in Figure 3(a); compared to that calculated at 50, 100, 150, and 200 GPa, a slight change is observed in the calculated bandgap decrease with increasing pressure, aligning with previous work for other related systems [31]. The energy bandgap of YHSe calculated at each pressure is as follows at 0 GPa (1.51 eV), 50 GPa (1.45 eV), 100 GPa (1.43 eV), 150 GPa (1.35 eV) and at 200 GPa (1.24 eV) in this work.

In transitioning from the analysis of band structure to the examination of DOS, we computed both the total DOS (TDOS) and projected DOS (PDOS) for YHSe across various pressures ranging from 0 to 200 GPa (see Figures 3(a), 3(b), 3(c), 3(d), and 3(e)). The Fermi-energy is set to be zero energy.

It is evident that YHSe exhibits semiconductor characteristics across various pressures up to 200 GPa, as evidenced by the absence of DOS at the Fermi level. This observation is consistent with the results of the energy band structure analysis at all pressures in this work. Hence, according to this study, it is important to note that YHSe exhibits semiconducting behavior. This characteristic is significant for understanding its potential applications in electronic devices and highlights its suitability for certain semiconductor-based technologies.

For more theoretical insight, the DOS of individual atoms Y, Se, and H in the YHSe structure are observed and depicted in Figure 3(a). In projected DOS analysis, in the YHSe, at 0 GPa, Se atoms contribute more to the TDOS than Y and H atoms in the valence band. Furthermore, Se-2p states contribute more than Se-3d states, with the majority of the DOS near the Fermi level attributed to Se-2p states. Conversely, in the YHSe system, Y-atoms contribute more to the TDOS than Se and H atoms in the conduction band. Additionally, Y-3d states contribute more than Y-5p states, and Se-3d states contribute more than Se-2p states, with the majority of the DOS near the Fermi level attributed to Y-3d states in the conduction band. This happens for all pressures, but the overlap between orbitals varies at different pressures in this work. In Figure 3(a), Se-3d bands overlap with Se-2p bands from 4.39 to 6.025 eV and from 6.35 to 8.305 eV. Again, Y-3d bands overlap with Se-3d bands at 7.28 −7.299 eV and 9.27–9.47 eV. This indicates Se-3d and Y-3d hybridization forming covalent bonds. At 150 GPa, Se-3d and Se-2p bands overlap from 6.86 to 9.043 eV. Finally, at 200 GPa in Figure 3(e), the two orbital overlap from 7.814 to 8.96 eV. On the other hand, Y-3d bands overlap with Se-3d at −5.0 to 8 eV and −3.19 to −4.387 eV. Overall, the TDOS near the Fermi surface N (ε_F) of YHSe decreases with increasing pressure, which is consistent results with a related system of previous work [32].

3.3. Vibrational Analysis. The phonon dispersions and projected phonon densities of states for YHSe are displayed in Figure 5 across various pressure conditions. The absence of any imaginary frequencies within the BZ confirms the dynamic stability of the YHSe system. Herein, our results demonstrated that YHSe is dynamically stable at a pressure of 0 GPa as shown in Figure 5(a). Moreover, we have calculated the phonon dispersion at pressures of 0, 50, 100, 150,

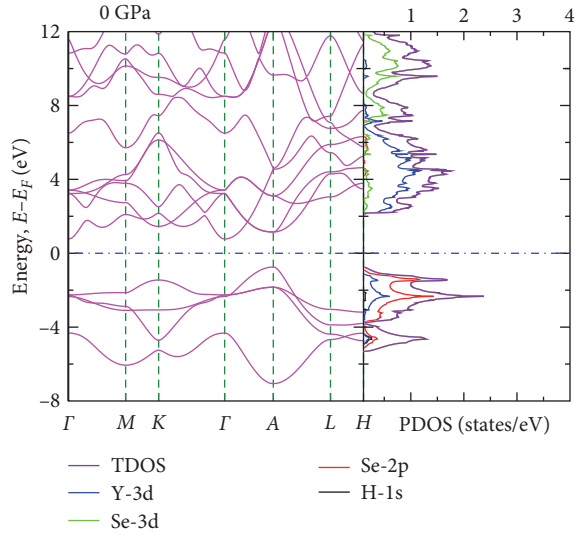

(a)

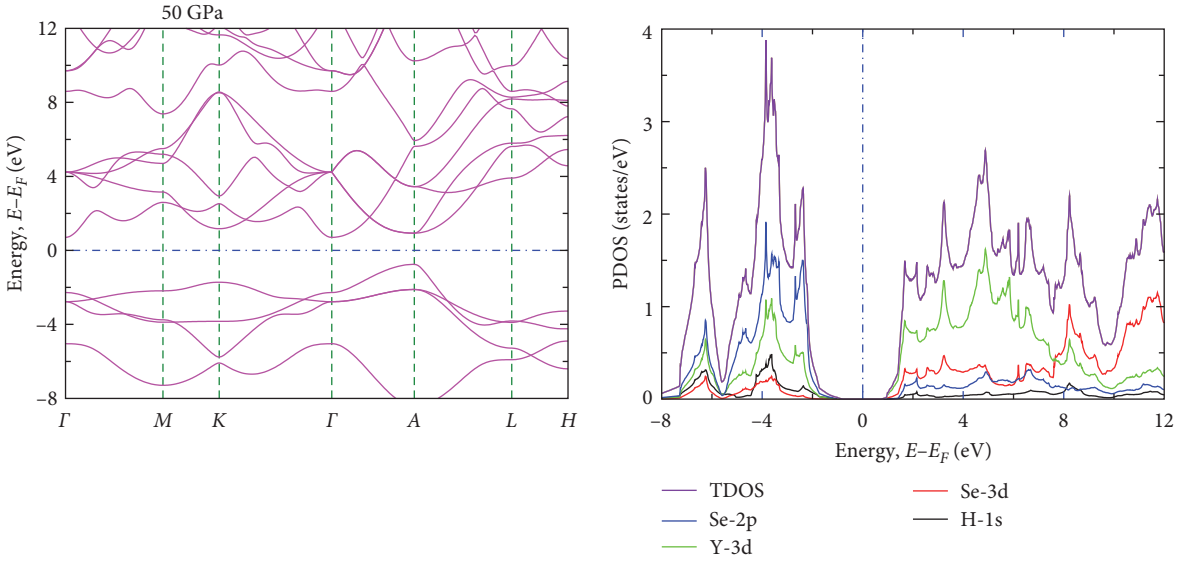

(b)

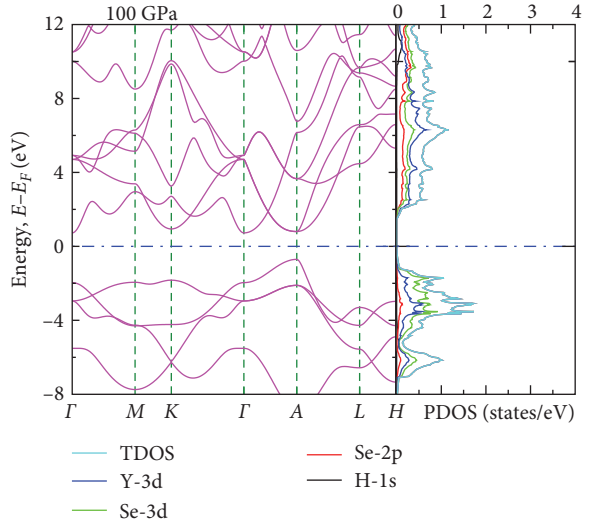

(c)

Figure 3: Continued.

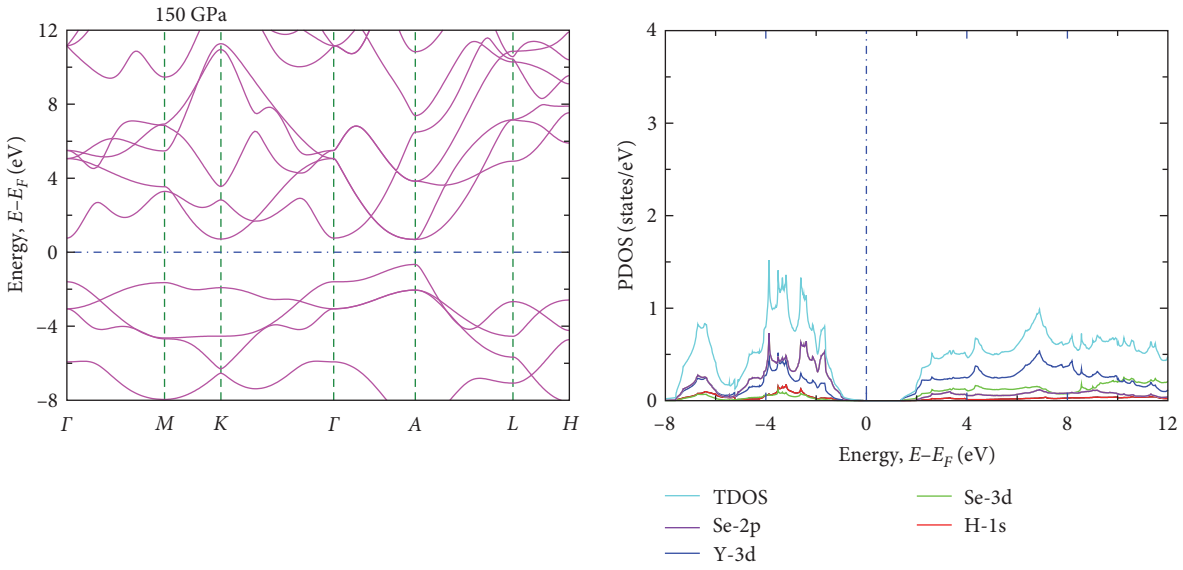

(d)

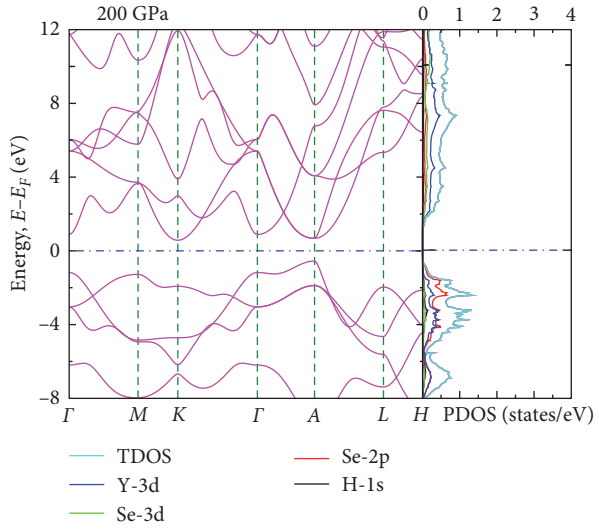

(e)

Figure 3: The calculated band structure and projected density of states (PDOS) of hexagonal structure with space group P$\bar{6}$m2 yttrium hydrogen selenide are presented at different pressures: (a) 0 GPa, (b) 50 GPa, (c) 100 GPa, (d) 150 GPa, and (e) 200 GPa.

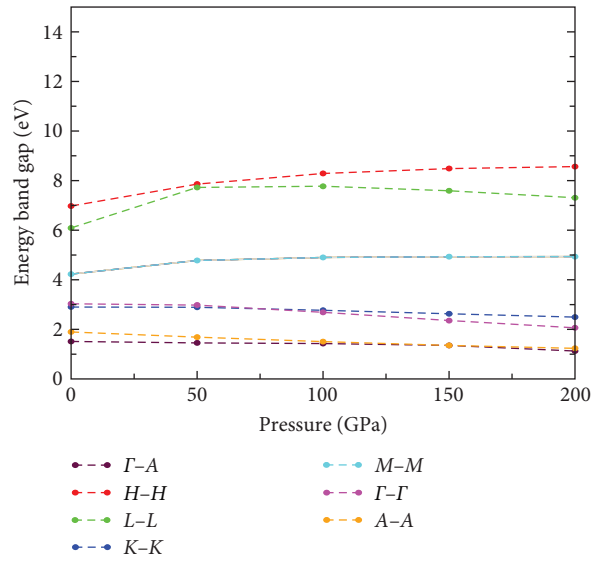

Figure 4: The calculated main Energy gaps of yttrium hydrogen selenide as a function of pressure.

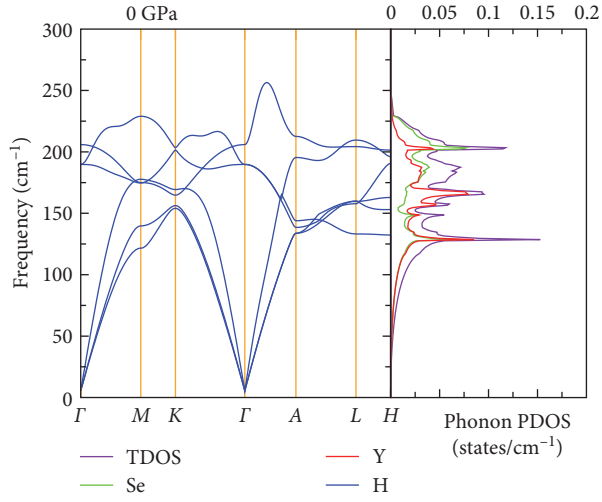

(a)

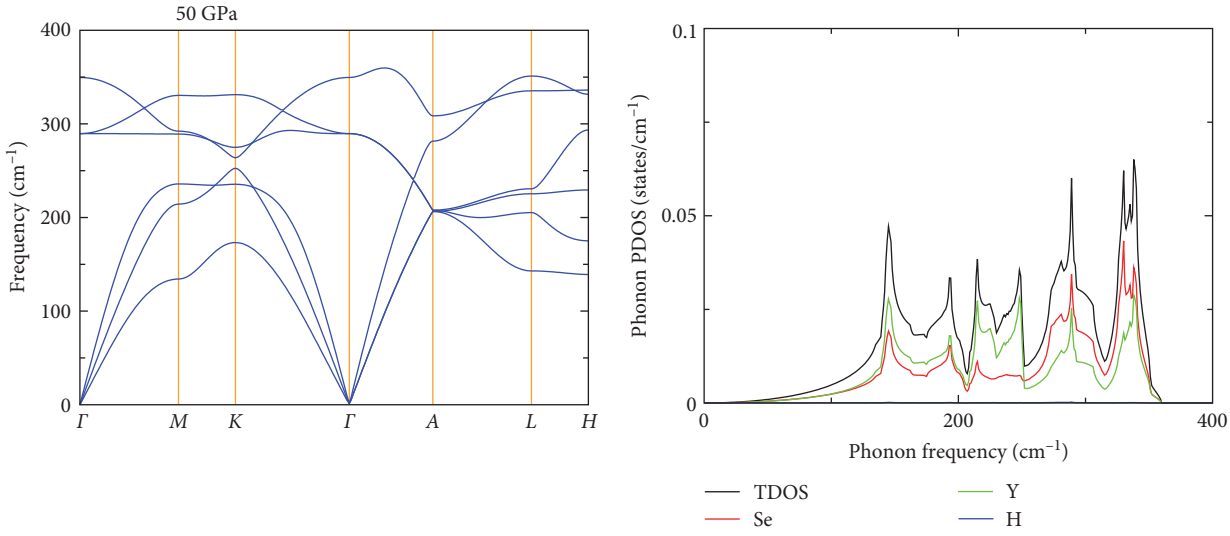

(b)

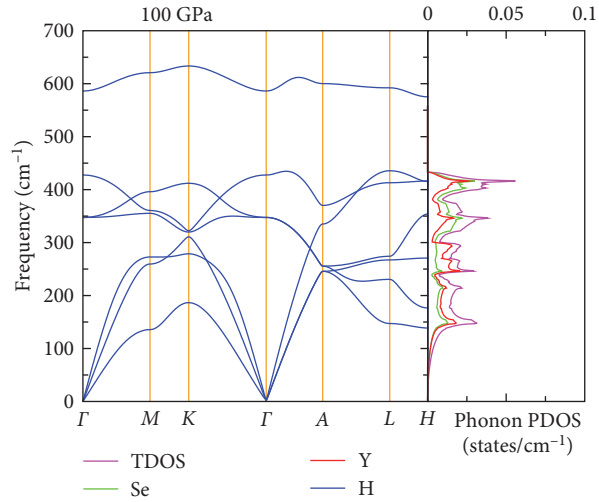

(c)

Figure 5: Continued.

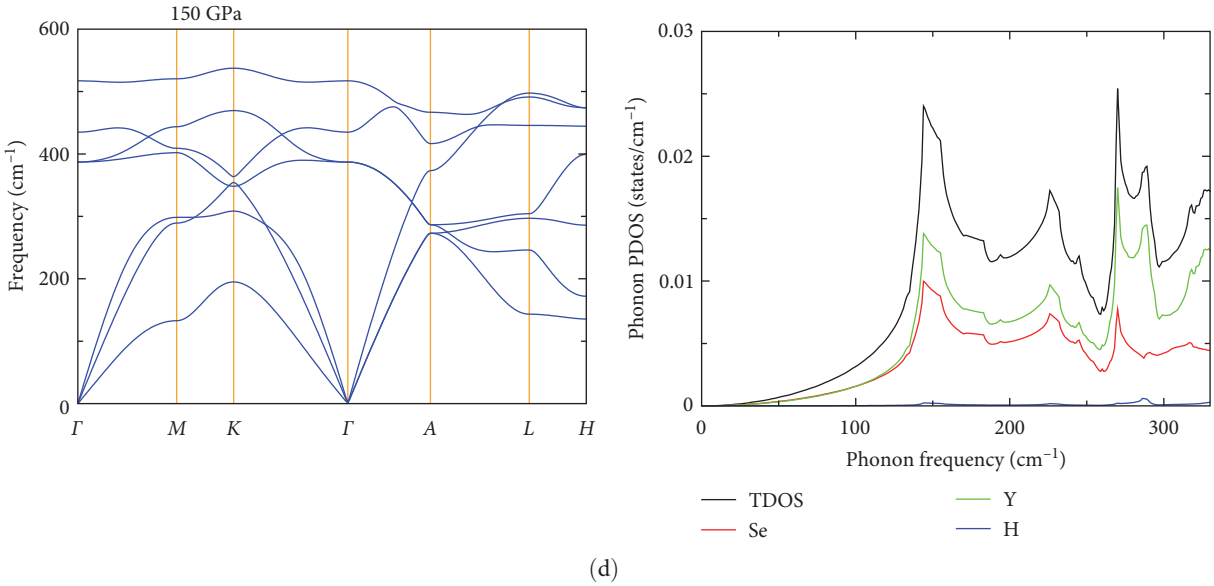

(d)

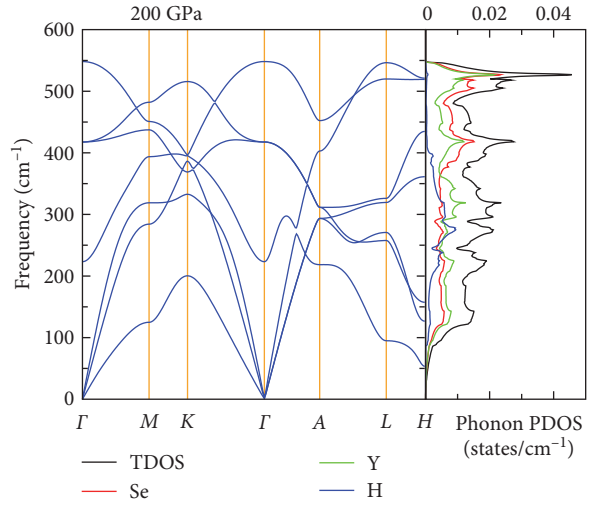

(e)

Figure 5: The phonon dispersions and projected phonon densities of states (PhDOS) for hexagonal structure with space group P$\bar{6}$m2 yttrium hydrogen selenide under different pressure: (a) 0 GPa; (b) 50 GPa; (c) 100 GPa; (d) 150 GPa; (e) 200 GPa.

Table 2: Phonon frequencies along high symmetry lines for hexagonal YHSe at 0 GPa.

High symmetry point	Phonon frequency (cm^{-1})
Γ:	209, 189.77
M:	116.18, 134.29, 172.25, 174.64, 175.05, 228.97
K:	148.59, 150.83, 163.89, 164.81, 201.20, 203.33
A:	128.29, 138.48, 195.44
L:	77, 127.74, 154.23, 154.58, 157.79, 166, 204.29, 209.61
H:	126.85

and 200 GPa and it is found that YHSe is dynamically stable. The phonon dispersion curves ω (q), depicted in Figures 5(a), 5(b), 5(c), 5(d), and 5(e), represent the relationship between phonon frequency and wave vector offering insights into the material's vibrational behavior across different momentum states. The phonon DOS F (ω), in Figure 5, at different pressures illustrates the distribution of phonon frequencies within the YHSe material, providing a comprehensive view of its vibrational spectrum.

The distinctive structure observed in the phonon spectrum, as highlighted in Figures 5(a), 5(b), 5(c), 5(d), and 5(e), is a direct consequence of the varying atomic masses of Y, Se, and H within the material. The phonon DOS of YHSe reveals that the low-frequency vibrations are predominantly dominated by the heavier Y-atoms, while the lighter Se-atoms, followed by H-atoms, contribute significantly to the high-frequency modes. This variance leads to the delineation of three distinct regions in the partial phonon DOS F (ω), each predominantly influenced by the vibrations of specific atomic species. In particular, the lower frequency segment is dominated by Y vibrations, followed by predominant Se

phonon branches, while the higher frequency range is significantly influenced by H atoms, contributing to higher frequencies due to their lighter mass [28].

At a pressure of 0 GPa, Figure 5(a), signifying the absence of external pressure, the peak phonon DOS is roughly 0.15 states/cm^{-1}. The DOS of phonons, which are quantized vibrational energy units in this material, is indicated by this value. The phonon DOS shows three different peaks in the frequency range of 125–215 cm^{-1} at this pressure. These peaks line up with particular vibrational modes of the material. The largest peak among these reaches a DOS of about 0.15 states/cm^{-1}. Nonetheless, the phonon DOS decreases from about 150 to 175 cm^{-1} in frequency. This decline implies that there are fewer vibrational modes available in this frequency range.

Then, the phonon DOS begins to rise again when the frequency rises over 175 cm^{-1} and gets closer to 220 cm^{-1}. The phonon DOS varies significantly when the pressure rises to 50 GPa (Figure 5(b)). There is a noticeable reduction in the peak phonon density; the initial peak is now observed at about 0.048 states/cm^{-1}. Concurrently, the next peaks show a slow rise in density as they go to higher frequencies, now between 300 and 400 cm^{-1}. This shift toward higher frequencies is consistent with the earlier research for a similar system and shows that the material's vibrational energy has been redistributed in response to the increased pressure [33].

The material's vibrational properties at high pressures are reflected by the four distinct peaks in the phonon DOS at 100 GPa (Figure 5(c)). The first peak appears in the 100–200 cm^{-1} frequency region, which corresponds to low-frequency vibrational modes. It shows a comparatively larger phonon DOS in this frequency range since it is marginally higher than the peak that follows. The second peak, which indicates a shift to intermediate-frequency vibrational modes, appears after the first peak and occurs in the 200–300 cm^{-1} frequency range. It has a somewhat lower density than the first peak, but as the frequency rises, the phonon density gradually increases.

The third peak, denoting an additional rise in density, emerges in the frequency range of 300–400 cm^{-1}, signifying an additional displacement toward elevated frequencies. The fourth peak, which is the highest of the four, is finally seen in the 400–450 cm^{-1} frequency region, which corresponds to high-frequency vibrational modes. This peak represents the material's capacity to support more vibrational modes at even higher frequencies when subjected to increased pressure. In a similar vein, the phonon DOS decreases dramatically to 0.024 states/cm^{-1} at 150 GPa (Figure 5(d)).

The material's vibrational behavior is represented by three separate peaks in the phonon DOS, which ranged in frequency from 100 to 350 cm^{-1} within this pressure regime. At a frequency of 150 cm^{-1}, the first peak becomes clearly visible, and its associated phonon DOS is 0.024 states/cm^{-1}. However, the DOS decreased as one moved closer to the second peak. The DOS then increases again as one approaches the third peak, suggesting that higher-frequency vibrational modes are once again available. The pressure's influence on the phonon dispersion curves of YHSe along specific high symmetry lines in the BZ, as shown in Figure 5. Initially, at 0 GPa pressure, the computed phonon dispersion curves closely match those obtained from inelastic neutron scattering measurements [34].

The investigation outlines key points regarding YHSe in this study, which are delineated in Table 2 and align with reported values of inelastic neutron scattering measurements at ambient pressure [34].

As depicted in Figure 5(b), as pressure increases, there is an observable tendency for phonon branches to move toward higher frequency ranges. However, the degree of this shift differs at various locations within the BZ. Figure 5(b) illustrates that at a pressure of 50 GPa, the frequency at each point on Γ, M, K, A, L, H surpasses that at each corresponding point when the pressure is at 0 GPa. Specifically, at 50 GPa, the frequency at the Γ-point ranges from 289.64 to 349.63 cm^{-1} at M from 134.28 to 330.45 cm^{-1}, at K from 173.27 to 331.21 cm^{-1}, at A from 206.41 to 308.56 cm^{-1}, and at L from 142.93 to 351.14 cm^{-1}. According to Figure 5(c), as the pressure increases to 100 GPa, there's a consistent trend of frequency raise observed across all points on Γ, M, K, A, L, and H, resembling the behavior observed at 50 GPa. However, at this heightened pressure, a distinct feature emerged one longitudinal optical branch diverges significantly from the rest of the optical phonons, showcasing a notably higher frequency. The frequencies associated with this distinct longitudinal optical phonon at each high symmetry point within the BZ are as follows: Γ: 586.65 cm^{-1}, M: 620.72 cm^{-1}, L: 592.12 cm^{-1}, K: 620.73 cm^{-1}, A: 600.11 cm^{-1}, and H: 575.06 cm^{-1}.

The phonon frequencies at each high symmetry point on K in the BZ (see Figure 6(b)) increased monotonically with pressure up to 200 GPa. This suggests that under increasing pressure, the phonon frequencies at K-high symmetry point's exhibit a monotonic increased up to 200 GPa. The findings of this investigation are aligned with previously reported data for related systems [35]. This behavior indicates a stiffening of the lattice dynamics under pressure. Phonon frequencies are related to the force constants between atoms in a crystal lattice. As pressure is applied, the interatomic distances decrease, leading to increased force constants and, consequently, higher phonon frequencies [36].

However, as shown in Figure 6(a), at 100 GPa, the frequency at the M point for the acoustic phonon is 135.59 cm^{-1}, and at 150 GPa, it decreases to 132.84 cm^{-1} further decreasing to 124.15 cm^{-1} at 200 GPa. Similarly, at 100 GPa, the frequency at the L-point for the acoustic phonon is 147.13 cm^{-1}, and at 150 GPa, it decreases to 143.27 cm^{-1}, further decreasing to 94.96 cm^{-1} at 200 GPa. Additionally, at 100 GPa, the frequency at the H-point for the acoustic phonon is 138.58 cm^{-1}, and at 150 GPa, it decreases to 135.49 cm^{-1}, further decreasing to 53.46 cm^{-1} at 200 GPa. Furthermore, the frequency at 150 GPa at the A-point for the acoustic phonon is 273.03 cm^{-1}; it decreases to 218.49 cm^{-1} at 200 GPa. The frequency at 150 GPa at the Γ-point is 387.03 cm^{-1} then decrease to 223.25 cm^{-1} at 200 GPa. This transition from an increase to a decrease in frequency as pressure raise from zero to 150 GPa suggests that the Gruneisen parameters at these points will become negative. This

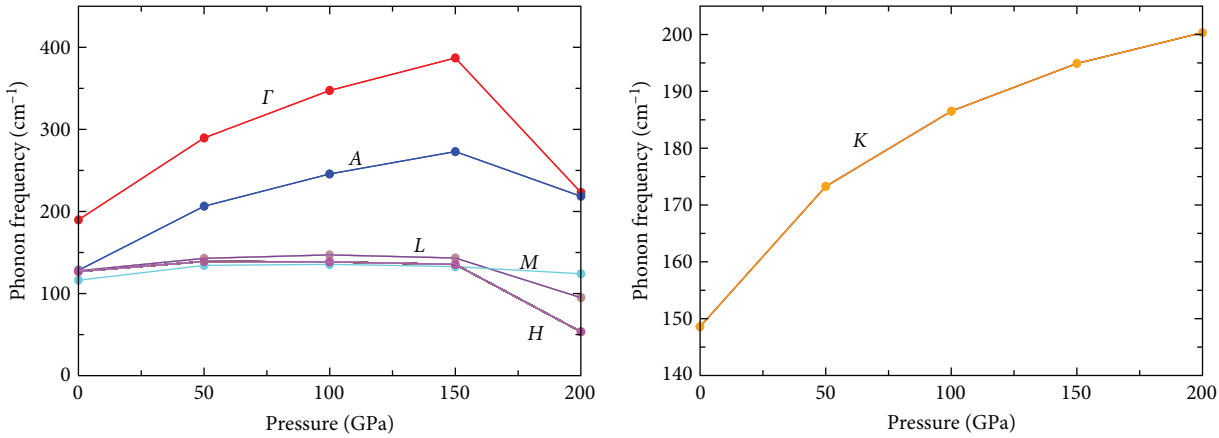

FIGURE 6: Pressure dependence of the phonon frequency of hexagonal structure with space group P$\bar{6}$m2 YHSe at high symmetry point (a) Γ, M, A, L, and H and (b) K.

conclusion is consistent with previously reported results for the related systems.

3.4. Superconducting Properties. In this work, the properties of superconductivity in the chosen structures can be effectively examined through EPC $\lambda(\omega)$ calculations. The calculated nonmonotonic dependence of the critical temperature (T_c) (Figure 7(a)) and EPC parameter, $\lambda(\omega)$ (Figure 7(b)) on external pressure in YHSe reveals intriguing insights into its superconducting properties under extreme conditions. The T_c of YHSe, the material's superconducting transition temperature under normal circumstances is 28 K at atmospheric pressure (0 GPa). Superconducting critical temperature (T_c) first decreases to 24.78 K at 50 GPa when external pressure increases, indicating a suppression of superconductivity. This reduction is similar with the trend of the prior work for the analogous system and may be caused by the compression of the crystal lattice, which alters the electronic band structure and weakens Cooper pairing [28].

As the pressure is raised to 100 GPa, T_c decreases even more to 15.8 K, suggesting that superconductivity is still being suppressed. The decrease in T_c indicated that the material's electrical characteristics are changed by the applied pressure, resulting in less strong superconducting activity [37]. Unexpectedly, there is a reversal beyond 100 GPa, and T_c begins to rise. T_c marginally increases to 15.9 K at 150 GPa, suggesting that superconducting may be enhanced or restored under extreme pressure scenarios. Our analysis shows that, among other previously reported hydrogen-based superconductors [22], the relationship between the critical temperature (T_c) and pressure (P) consistently trends beyond 100 GPa.

All of the high superconducting critical temperature T_c systems accessed under extreme pressure and thus reported are hydrogen-rich materials, in which the superconductivity is driven by strong EPC to the high-frequency hydrogen phonon modes [38, 39]. Thus, Figure 7(a) shows that the critical temperature (T_c) increases to 31.64 K at an extreme pressure of 200 GPa, indicating a significant enhancement of superconductivity at extreme pressure. This trend in the relationship between pressure and T_c at extreme conditions is consistent with the findings of the prior study for related hydrogen-rich materials [16]. In the YHSe system, the T_c grows monotonically from 15.8 K at 100 GPa to 31.64 K at 200 GPa. This rising behavior points to intricate structural changes or electronic transitions that support high-pressure superconductivity, a pattern that is consistent with past reports of superconductivity based on hydrogen [40].

The extreme pressure may lead to a lattice configuration that optimally supports strong EPC [38, 41]. This configuration could enhance the efficiency of Cooper pair formation, leading to an increase in T_c. The significant increase in $\lambda(\omega)$ to 2.63 supports this notion, indicating a remarkable enhancement of electron–phonon interactions conducive to superconductivity. In our investigation, we have found that despite the decrease in the DOS near the Fermi level (Figures 3(a), 3(b), 3(c), 3(d), and 3(e)) as the pressure raises the efficiency of EPC may increase at higher pressures due to change in lattice dynamics/phonon frequency or electronic structure [39, 42].

In this work, electron-lattice vibration interactions may become more efficient, leading to $\lambda(\omega) = 2.63$ at 200 GPa, which could lead to enhanced superconductivity and a higher T_c as compared to low critical temperature superconducting materials in the YHSe system, even though the number of accessible electronic states near the Fermi level decreases with pressure.

At very high pressures, the lattice structure of solid may undergo stabilization, which can promote a more favorable environment for superconductivity [39]. This stabilization may reduce lattice vibrations or distortions that could impede Cooper pair formation, thereby boosting T_c. This means that the interactions between electrons and lattice vibrations (phonons) become stronger under extreme pressure conditions, leading to an increase in T_c [38, 40]. Consequently, even in circumstances where the density of accessible electronic states in the YHSe system is decreased, improved EPC can encourage the production of Cooper pairs in the current work. This indicates that the decreases

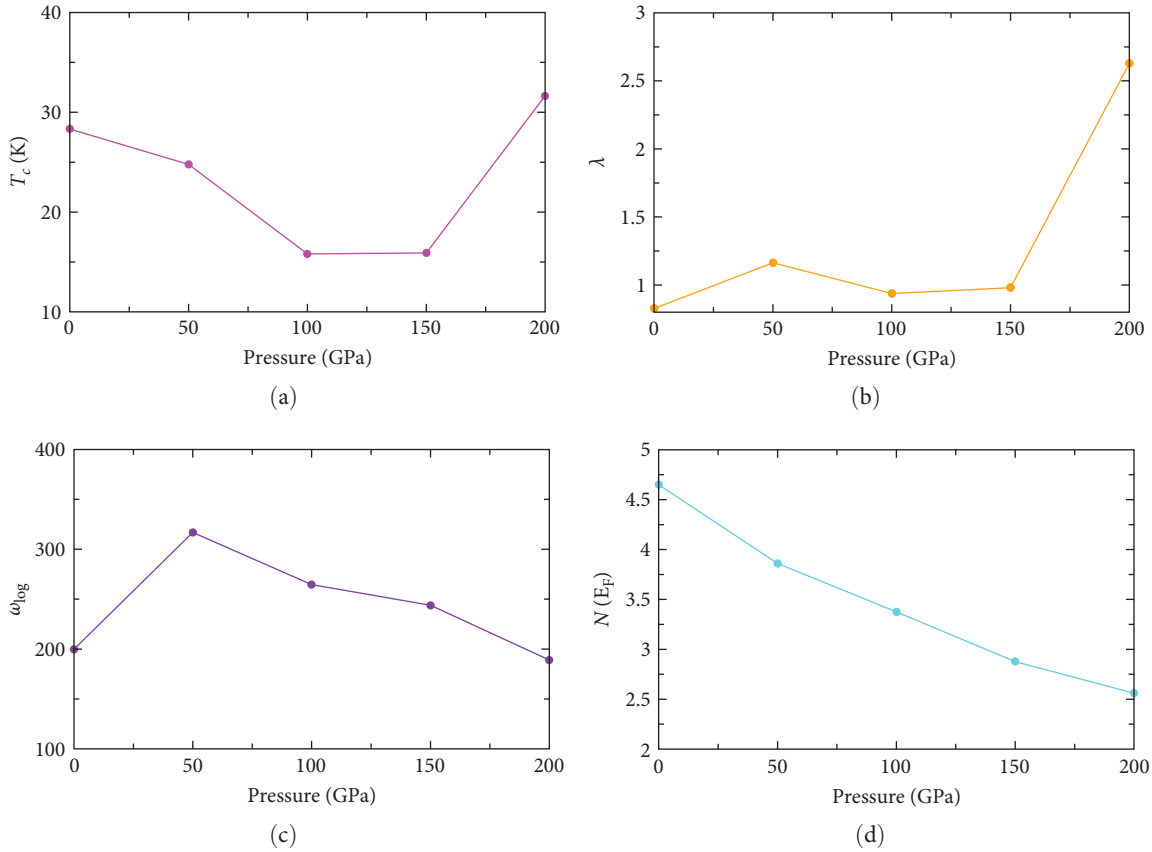

FIGURE 7: (a) Calculated critical temperature superconductivity of space group P$\bar{6}$m2 hexagonal of YHSe. (b) Calculated the integrating of lambda, $\lambda(\omega)$ of P$\bar{6}$m2 of YHSe. (c) Calculated the logarithmic average phonon frequency $\omega_{\log}$ of P$\bar{6}$m2 hexagonal YHSe. (d) Calculated total density of states DOS near the Fermi level as a function of pressure for YHSe.

in the electronic density of the state in the current investigation are effectively compensated by the rise in EPC. The EPC parameter (λ) at ambient pressure (0 GPa) is calculated to be 0.83, indicating moderate electron–phonon interactions since ($\lambda < 1$). Through their facilitation of Cooper pair production, these interactions are essential in mediating superconductivity.

As the applied pressure increases to 50 GPa (Figure 8), it results in an increase in λ to 1.16, suggesting enhanced EPC. This is indicative of a stronger electron–phonon interaction at this pressure, as the EPC parameter exceeds one since $\lambda > 1$.

However, from Figure 8, increasing the pressure to 100 GPa leads to a reduction in λ to 0.94, indicating a weakening of electron–phonon interactions since ($\lambda < 1$). The lattice distortion induced by the high pressure might lead to changes in the phonon spectrum that counteract the increase in EPC [42]. The overall EPC λ shifts from 1.16 down to 0.94 between 50 and 100 GPa and with the Coulomb pseudo potential ($\mu^* = 0.10$) to a reduction of T_c from 24.78 to 15.8 K between 50 and 100 GPa. Hence, the reduction of EPC good agreement with the reduction of T_c in between the pressure of 50 and 100 GPa in the present work.

According to Figures 7(a) and 7(b), further increasing the pressure beyond 100 GPa results in a notable increase in (λ); interestingly, beyond 100 GPa as pressure increases, the total

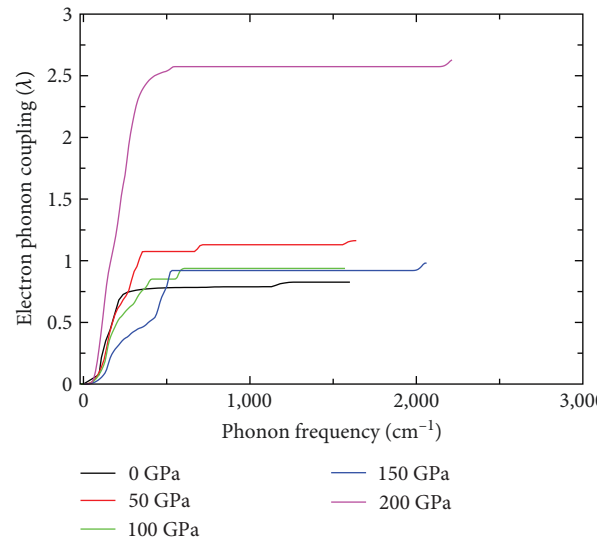

FIGURE 8: Frequency distribution of the electron–phonon coupling parameter, $\lambda(\omega)$ with space group P$\bar{6}$m2 hexagonal YHSe under different pressure calculated as, $\lambda(\omega) = 2\int_0^{\infty} \frac{\alpha^2 F(\omega)}{\omega} d\omega$.

λ increases monotonously, consistent with the increases of T_c calculated by this work. At 150 GPa, λ rise to 0.98 indicating a resurgence in EPC but still weak electron phonon interaction since $\lambda < 1$.

These band structure effects may lead to an enhancement of EPC and an increase in λ despite the overall challenging conditions at extreme pressures [41]. Thus, changes in the electronic band structure induced by pressure in YHSe at higher pressures could influence the distribution of electronic states and their coupling to lattice vibrations.

The EPC parameter increases significantly ($\lambda = 2.63 > 1$) at an extreme pressure of 200 GPa (see Figure 8), suggesting a notable enhancement of electron–phonon interactions. This enhancement is probably responsible for the calculated increase in the critical temperature (T_c) at 200 GPa in the YHSe with $T_c = 31.64$ K.

In transitioning from the discussion of electron–phonon strength (λ) to the logarithmic average phonon frequency ($\omega_{\log}$), our investigation uncovers a compelling nonlinear trend under increasing pressure. The logarithmic average phonon frequency exhibits a notable increase from 199.83 to 316.89 K at 50 GPa, indicating heightened atomic interactions and a transition toward stiffer atomic arrangements. This initial rise underscores the material's responsiveness to external pressure, suggesting a capacity for structural adaptation in response to compression. Subsequently, as pressure continues to increase, logarithmic average phonon frequency ($\omega_{\log}$) exhibits fluctuations, hovering within the range of 264 −250 K between 100 and 150 GPa (Figure 7(c)). However, as pressure intensifies further, the logarithmic average phonon frequency experiences a noticeable decrease, dropping rapidly to 189.060 K at 200 GPa. Figure 7(c) illustrates that the logarithmic average phonon frequency increase at low pressures reaches a maximum at 50 GPa and then decreases to 189.06 K at 200 GPa.

Moreover, in this study the results of Eliashberg spectral function $\alpha^2F(\omega)$ and integrated electron–phonon coupling constant as a function of phonon frequency $\lambda(\omega)$ were calculated at 0, 50, 100, 150, and 200 GPa. The phonon spectrum or Eliashberg spectral function, $\alpha^2F(\omega)$ and cumulative electron–phonon coupling $\lambda(\omega)$ of YHSe were calculated to investigate the lattice dynamics and electron–phonon interactions for this system. The Eliashberg spectral function denoted as $\alpha^2F(\omega)$ serves as a valuable indicator for assessing the overall influence of induced pressure effects on the EPC within a material as previously experimental confirmed for different system [37]. This Eliashberg spectral function essentially characterizes the strength of the electron–phonon interaction at different phonon frequencies [37].

According to Figures 9(a), 9(b), 9(c), 9(d), and 9(e), when examining, $\alpha^2F(\omega)$ one can observe peaks at certain frequencies in YHSe system. These peaks correspond to the dominant phonon modes that contribute significantly to the EPC, $\lambda(\omega)$. At ambient pressure (Figure 9(a)), the medium and greatest peaks in $\alpha^2F(\omega)$ are observed within a specified frequency range, typically between 143 and 220 cm^{-1}, with corresponding peak values of 0.38 and 0.67. This range illustrates the frequencies at which the most significant electron–phonon interaction occurs during normal conditions.

According to Figure 9(a), the findings clearly indicated that at current pressure settings, no additional noticeable peaks appear beyond the range of 143–220 cm^{-1}, showing

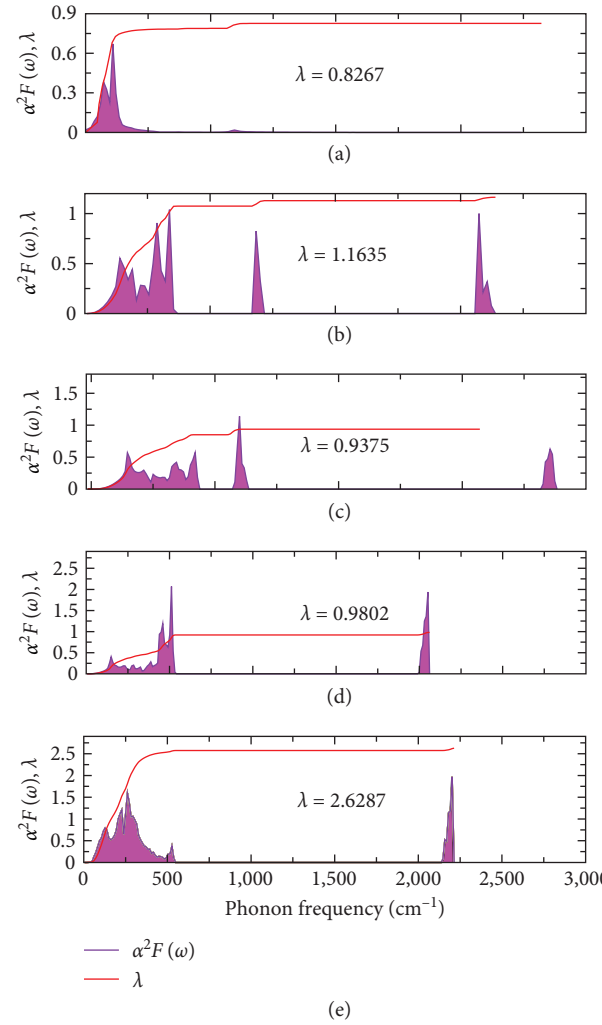

FIGURE 9: The Eliashberg spectral function and the integrating of lambda, $\lambda(\omega)$ for hexagonal of YHSe are calculated at (a) 0, (b) 50, (c) 100, (d) 150, and (e) 200 GPa.

that changes in phonon dispersion are insufficient to generate new dominant coupling frequencies. Moreover, increased pressure causes additional peaks in the Eliashberg spectral function, $\alpha^2F(\omega)$ specifically, at 50 GPa; five distinct peaks emerge in the Eliashberg spectral function $\alpha^2F(\omega)$.

The first three peaks are located within the frequency range of 140–340 cm^{-1} with corresponding Eliashberg function values ranging from 0.5 to 1.05. The first, second, and third peak is situated at a phonon frequency of 140, 288.28, and 337.7 cm^{-1} with an associated Eliashberg spectral function value of 0.553, 0.906, and 1.04, respectively.

Furthermore, two additional peaks manifest at higher frequencies. The fourth and fifth peaks appear at a frequency of 683.64 and 1,573.20 cm^{-1} with an Eliashberg spectral function value of 0.83 and 1, respectively. These observations indicate that under the applied pressure of 50 GPa, the phonon dispersion undergoes significant alterations, resulting in the appearance of new dominant phonon modes contributing to EPC, $\lambda(\omega)$ as compared to 0 GPa.

Clearly from Figure 9(c), as the pressure further increased to 100 GPa, a similar trend in the Eliashberg spectral function is observed with five distinct peaks and two shoulder peaks appearing at different phonon frequency ranges compared to both the ambient pressure and the 50 GPa conditions. The first three peaks are observed within the phonon frequency range of 146–422 cm^{-1}. Specifically, the first, second, and third peak occurs at a phonon frequency of 146.32, 344.57, and 420.53 cm^{-1}, exhibiting an Eliashberg spectral function value of 0.297, 0.419, and 0.572, respectively. Moreover, two additional peaks are observed at higher frequencies. The fourth and fifth peaks are situated at a phonon frequency of 599.45 and 1,855 cm^{-1} demonstrating an Eliashberg spectral function value of 1.14 and 0.626, respectively. These peaks indicate the presence of dominant phonon modes contributing to EPC within the YHSe material. As the pressure increases to 150 GPa, the Eliashberg spectral function continues to reveal significant alterations in the material's EPC behavior (Figure 9(d)). At this pressure, four distinct peaks and shoulder peaks appear at different phonon frequency ranges. The first peak is located at a phonon frequency of 149.83, 459.82 cm^{-1} with an Eliashberg function of 0.40 and 1.19, respectively. The Eliashberg spectral function value for this peak is notably higher at 1.19, indicating a significant enhancement in the electron–phonon interaction strength (λ) compared to the first peak. The third peak, observed at a phonon frequency of 511.48 cm^{-1}, represents another significant enhancement in EPC. With an Eliashberg spectral function value of 2.07, this peak signifies a particularly strong interaction between electrons and phonons at this frequency.

At a much higher phonon frequency of 2,051.10 cm^{-1}, the fourth peak is observed, indicating EPC interactions at even higher energy levels. The Eliashberg spectral function value associated with this peak is 1.94, indicating a significant coupling strength at this high frequency. According to Figure 9(e), as the pressure increases to 200 GPa, the Eliashberg spectral function continues to reveal significant alterations in the material's EPC behavior. At this pressure, five peaks emerge, each at a distinct phonon frequency, shows various electron–phonon interactions within this the material. The first, second, and third peaks appear at a phonon frequency of 128, 227, and 261 cm^{-1}, accompanied by a corresponding Eliashberg spectral function value of 0.79, 1.21, and 1.59, respectively. The fourth and fifth peaks appear at phonon frequency of 527 and 2,200 cm^{-1}, though with an Eliashberg spectral function value of 0.378 and 1.97, respectively.

Overall, the peak value of the Eliashberg function at each pressure shows electron–phonon interactions at those pressures that aligned with electron–phonon coupling in this study.

Furthermore, the Eliashberg functions for the YHSe compound at various pressures have been collected to visualize their relative positions concerning pressure, providing insight into the electron–phonon interaction (Figure 10). According to Figure 10, the Eliashberg function has the highest peak value at pressures of 150 and 200 GPa, among others; this shows that stronger electron–phonon interaction at these pressures.

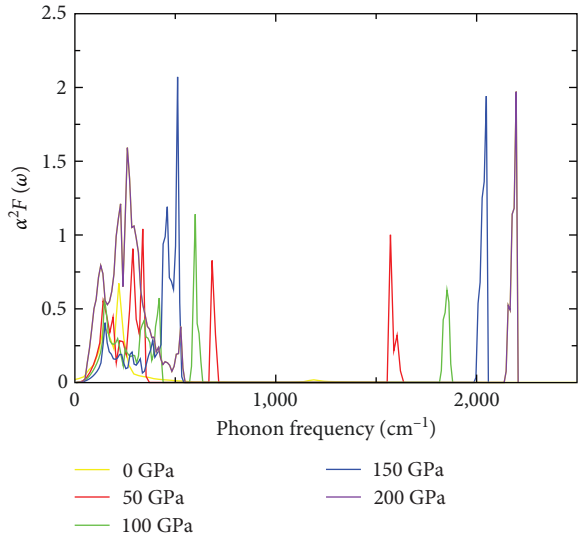

FIGURE 10: Eliashberg functions of YHSe for all pressures are gathered to visualize their relative evolution with pressure.

4. Conclusions

In this research work, a thorough examination of the electronic, phonon, and superconductivity properties of hexagonal YHSe with space group $P\bar{6}m2$ under varying pressure conditions is studied. The investigation revealed intriguing pressure-dependent behaviors in both the band structure and DOS, with the bandgap transitioning between indirect and direct characteristics at a certain high symmetry point as pressure increases. Despite these changes, YHSe maintains its semiconductor characteristics since the energy bandgap along Γ–A direction is in the range of 1.24–1.52 eV for all pressure ranges, and the bandgap gradually decreasing under pressure. Furthermore, the study delves into the vibrational properties of YHSe, showcasing shifts and changes in phonon dispersions and DOS under pressure. Importantly, YHSe remains dynamically stable across all pressure conditions, with phonon frequencies showing monotonic increases. Additionally, a transition from positive to negative Gruneisen parameters is observed at certain pressure points, indicating a shift in lattice dynamics under extreme pressure conditions.

Moreover, the investigation into superconducting properties under pressure reveals a complex interplay between structural dynamics, EPC, and superconductivity. The findings show that electrical and vibrational factors influence YHSe's superconducting properties, with pressure playing an important role in modifying these interactions. Understanding these complex interactions is critical for the creation and optimization of superconducting materials with improved performance and stability. Furthermore, the findings of this study have important implications for the design, production, and application of new materials with customized electrical, vibrational, and superconducting properties for advanced technological applications. Overall, this study contributes valuable insights into the behavior of YHSe under extreme conditions, paving the way for further exploration in experimental study.

Data Availability

The data that support the findings of the study are available within the article.

Conflicts of Interest

The authors declare that there are no conflicts of interest regarding the publication of this paper.

Authors' Contributions

All authors listed have made a substantial, direct, and intellectual contribution to the work and approved it for publication.

Acknowledgments

We gratefully acknowledge Adama Science and Technology University (ASTU) and Bule Hora University (Tadesse B.) for their support during this work.

References

[1] M. Tinkham, *Introduction to Superconductivity*, Courier Corporation, 2004.

[2] P.-G. De Gennes, *Superconductivity of Metals and Alloys*, CRC press, 2018.

[3] J. Linder and J. W. A. Robinson, "Superconducting spintronics," *Nature Physics*, vol. 11, no. 4, pp. 307–315, 2015.

[4] B. D. Josephson, "Possible new effects in superconductive tunnelling," *Physics Letters*, vol. 1, no. 7, pp. 251–253, 1962.

[5] A. Bergen, R. Andersen, M. Bauer et al., "Design and in-field testing of the world's first ReBCO rotor for a 3.6 MW wind generator," *Superconductor Science and Technology*, vol. 32, no. 12, Article ID 125006, 2019.

[6] M. R. Islam, Y. Guo, and J. Zhu, "A review of offshore wind turbine nacelle: technical challenges, and research and developmental trends," *Renewable and Sustainable Energy Reviews*, vol. 33, pp. 161–176, 2014.

[7] H. Thomas, A. Marian, A. Chervyakov, S. Stückrad, D. Salmieri, and C. Rubbia, "Superconducting transmission lines—sustainable electric energy transfer with higher public acceptance?" *Renewable and Sustainable Energy Reviews*, vol. 55, pp. 59–72, 2016.

[8] S. S. Kalsi, *Applications of High Temperature Superconductors to Electric Power Equipment*, John Wiley & Sons, 2011.

[9] J. A. Flores-Livas, L. Boeri, A. Sanna, G. Profeta, R. Arita, and M. Eremets, "A perspective on conventional high-temperature superconductors at high pressure: methods and materials," *Physics Reports-Review Section of Physics Letters*, vol. 856, pp. 1–78, 2020.

[10] N. W. Ashcroft, "Metallic hydrogen: a high-temperature superconductor?" *Physical Review Letters*, vol. 21, no. 26, pp. 1748-1749, 1968.

[11] J. Bardeen, L. N. Cooper, and J. R. Schrieffer, "Microscopic theory of superconductivity," *Physical Review*, vol. 106, no. 1, pp. 162–164, 1957.

[12] J. Bardeen, L. N. Cooper, and J. R. Schrieffer, "Theory of superconductivity," *Physical Review*, vol. 108, no. 5, pp. 1175–1204, 1957.

[13] E. Wigner and H. Huntington, "On the possibility of a metallic modification of hydrogen," *The Journal of Chemical Physics*, vol. 3, no. 12, pp. 764–770, 1935.

[14] W. Zhao, "Superconducting ternary hydrides: progress and challenges," *National Science Review*, vol. 11, Article ID nwad307, 2024.

[15] X. Feng, J. Zhang, G. Gao, H. Liu, and H. Wang, "Compressed sodalite-like MgH_6 as a potential high-temperature superconductor," *RSC Advances*, vol. 5, no. 73, pp. 59292–59296, 2015.

[16] S. Besedin, M. Eremets, I. Troyan, and A. Irodova, "Search for CaH_6 in X-ray diffraction measurements at pressures up 200 GPa," vol. 28, 2021.

[17] Y. Li, J. Hao, H. Liu, J. S. Tse, Y. Wang, and Y. Ma, "Pressure-stabilized superconductive yttrium hydrides," *Scientific Reports*, vol. 5, no. 1, Article ID 9948, 2015.

[18] F. Peng, Y. Sun, C. J. Pickard, R. J. Needs, Q. Wu, and Y. Ma, "Hydrogen clathrate structures in rare earth hydrides at high pressures: possible route to room-temperature superconductivity," *Physical Review Letters*, vol. 119, no. 10, Article ID 107001, 2017.

[19] D. V. Semenok, I. A. Troyan, A. G. Ivanova et al., "Superconductivity at 253K in lanthanum–yttrium ternary hydrides," *Materials Today*, vol. 48, pp. 18–28, 2021.

[20] A. P. Drozdov, P. P. Kong, V. S. Minkov et al., "Superconductivity at 250 K in lanthanum hydride under high pressures," *Nature*, vol. 569, no. 7757, pp. 528–531, 2019.

[21] Y. Yao and J. S. Tse, "Superconducting hydrogen sulfide," *Chemistry—A European Journal*, vol. 24, no. 8, pp. 1769–1778, 2018.

[22] A. Ghaffar, P. Song, K. Hongo, and R. Maezono, "High-T_c superconductivity of clathrate Y_3 EuH_{24}," arXiv Prepr. arXiv2205.05906, 2022.

[23] X. Zhang, Y. Zhao, and G. Yang, "Superconducting ternary hydrides under high pressure," *WIREs Computational Molecular Science*, vol. 12, no. 3, Article ID e1582, 2022.

[24] M. Ernzerhof and G. E. Scuseria, "Assessment of the Perdew–Burke–Ernzerhof exchange-correlation functional," *The Journal of Chemical Physics*, vol. 110, no. 11, pp. 5029–5036, 1999.

[25] H. J. Monkhorst and J. D. Pack, "Special points for Brillouin-zone integrations," *Physical Review B*, vol. 13, no. 12, pp. 5188–5192, 1976.

[26] B. G. Pfrommer, M. Côté, S. G. Louie, and M. L. Cohen, "Relaxation of crystals with the Quasi–Newton method," *Journal of Computational Physics*, vol. 131, no. 1, pp. 233–240, 1997.

[27] S. Baroni, S. de Gironcoli, A. D. Corso, and P. Giannozzi, "Phonons and related crystal properties from density-functional perturbation theory," *Reviews of Modern Physics*, vol. 73, no. 2, pp. 515–562, 2001.

[28] W. L. McMillan, "Transition temperature of strong-coupled superconductors," *Physical Review*, vol. 167, no. 2, pp. 331–344, 1968.

[29] O. Gunnarsson, D. Rainer, and G. Zwicknagl, "Screened interaction and Coulomb pseudo-potential in C_{60}," *International Journal of Modern Physics B*, vol. 06, no. 23n24, pp. 3993–4005, 2012.

[30] W. Setyawan and S. Curtarolo, "High-throughput electronic band structure calculations: challenges and tools," *Computational Materials Science*, vol. 49, no. 2, pp. 299–312, 2010.

[31] D.-K. Seo, N. Gupta, M.-H. Whangbo, H. Hillebrecht, and G. Thiele, "Pressure-induced changes in the structure and band gap of CsGeX3 (X = Cl, Br) studied by electronic band structure calculations," *Inorganic Chemistry*, vol. 37, no. 3, pp. 407–410, 1998.

[32] M.-Z. Huang, Y.-N. Xu, and W. Y. Ching, "Pressure dependence of the band structure, density of states, fermi surfaces, and optical properties of superconducting K_3C_{60}," *Physical Review B*, vol. 47, no. 13, pp. 8249–8259, 1993.
[33] J. M. Besson, "Pressure dependence of T_c and electron phonon interaction in $MBa_2Cu_3O_7$ systems," *Journal de Physique*, vol. 50, no. 12, pp. 1433–1443, 1989.
[34] J. Xie, S. P. Chen, J. S. Tse, S. de Gironcoli, and S. Baroni, "High-pressure thermal expansion, bulk modulus, and phonon structure of diamond," *Physical Review B*, vol. 60, no. 13, pp. 9444–9449, 1999.
[35] X.-J. Chen, V. Struzhkin, S. Kung, H.-K. Mao, R. Hemley, and A. Christensen, "Pressure-induced phonon frequency shifts in transition-metal nitrides," *Physical Review B*, vol. 70, no. 1, Article ID 14501, 2004.
[36] P. B. Allen and R. C. Dynes, "Superconductivity and phonon softening: II. Lead alloys," *Physical Review B*, vol. 11, no. 5, pp. 1895–1905, 1975.
[37] A. Sagar and R. C. Miller, "Study of band structure of intermetallic compounds by pressure experiments," *Journal of Applied Physics*, vol. 32, no. 10, pp. 2073–2078, 1961.
[38] D. Y. Kim, R. H. Scheicher, H.-K. Mao, T. W. Kang, and R. Ahuja, "General trend for pressurized superconducting hydrogen-dense materials," *Proceedings of the National Academy of Sciences*, vol. 107, no. 7, pp. 2793–2796, 2010.
[39] K. Tanaka, J. S. Tse, and H. Liu, "Electron–phonon coupling mechanisms for hydrogen-rich metals at high pressure," *Physical Review B*, vol. 96, no. 10, Article ID 100502, 2017.
[40] G. M. Eliashberg, "Interactions between electrons and lattice vibrations in a superconductor," *Soviet Phyics JETP*, vol. 11, no. 3, pp. 696–702, 1960.
[41] B. Lorenz and C. W. Chu, "High pressure effects on superconductivity," in *Frontiers in Superconducting Materials*, pp. 459–497, Springer, 2005.
[42] A. Congeduti, P. Postorino, E. Caramagno, M. Nardone, A. Kumar, and D. D. Sarma, "Anomalous high pressure dependence of the Jahn–Teller phonon in $La_{0.75}\,Ca_{0.25}\,MnO_3$," *Physical Review Letters*, vol. 86, no. 7, pp. 1251–1254, 2001.